

# On the stability of super-heavy nuclei

K. Pomorski,<sup>1,\*</sup> B. Nerlo-Pomorska,<sup>1</sup> J. Bartel,<sup>2</sup> and C. Schmitt<sup>2</sup>

<sup>1</sup>*Uniwersytet Marii Curie Skłodowskiej, Katedra Fizyki Teoretycznej, 20031 Lublin, Poland*

<sup>2</sup>*IPHC, Université de Strasbourg-CNRS, 67037 Strasbourg, France*

(Dated: September 11, 2021)

The potential-energy surfaces of an extended set of heavy and super-heavy even-even nuclei with  $92 \leq Z \leq 126$  and isospins  $40 \leq N - Z \leq 74$  are evaluated within the recently developed Fourier shape parametrization. Ground-state and decay properties are studied for 324 different even-even isotopes in a four-dimensional deformation space, defined by non-axiality, quadrupole, octupole, and hexadecapole degrees of freedom. Nuclear deformation energies are evaluated in the framework of the macroscopic-microscopic approach, with the Lublin-Strasbourg-Drop model and a Yukawa-folded mean-field potential. The evolution of the ground-state equilibrium shape (and possible isomeric, metastable states) is studied as a function of  $Z$  and  $N$ . Alpha-decay  $Q$ -values and half-lives, as well as fission-barrier heights, are deduced. In order to understand the transition from asymmetric to symmetric fission along the Fm isotopic chain, the properties of all identified fission paths are investigated. Good agreement is found with experimental data wherever available. New interesting features about the population of different fission modes for nuclei beyond Fm are predicted.

PACS numbers: 24.75.0+i, 25.85.-w, 21.10.Gv, 31.50.-x

## I. INTRODUCTION

The properties of nuclei at the edge of the nuclear chart and consequently at the limit of stability, namely in the region of very-heavy (VHE) and super-heavy (SHE) elements, are of paramount interest, since they constitute a stringent test of any nuclear model. While many theories are nowadays indeed able to achieve a fair description of nuclear masses for nuclei on and close to the  $\beta$ -stability line, these can substantially deviate when moving to the SHE region. Apart from the fundamental interest to achieve a better understanding of the involved physics, the predictive power of these theoretical approaches is of capital importance to guide the challenging experimental quest for the so-called SHE island of stability.

Models used in this field can be essentially classified into two categories, the self-consistent microscopic approach rooted, on a more or less fundamental level (effective interactions, meson fields, quark degrees of freedom, ...) in the underlying nuclear force, and the macroscopic-microscopic model that describes the nucleus as a charged liquid drop with quantal (shell and pairing) corrections. Even though the self-consistent microscopic theory has been developed substantially, its achievements depend strongly on the specific nuclear interaction used (see e.g. Ref. [1]). The large computing-resources required are, in addition, still a limiting factor for systematic investigations. The macroscopic-microscopic approach, on the other hand, has proven to constitute a reliable method for addressing a very wide variety of questions in the field, and this with impressively good accuracy [2].

The present work is a continuation of our previous investigation [3] in which we have introduced a new, powerful and rapidly converging description of nuclear deformations based on a Fourier decomposition of the nuclear shape. Combined with a well-established macroscopic-microscopic model, nuclear deformation-energy landscapes have been investigated for preactinides and actinides ( $78 \leq Z \leq 94$ ) and shown to be in good agreement with the available experimental data. The present study proposes to extend the application of the model into the less-known SHE region.

The innovative Fourier shape parametrization and the main features of the macroscopic-microscopic potential-energy calculation are discussed in section II. The results of our calculations are presented in section III, discussing first the equilibrium deformations and their dependence on  $Z$  and  $N$ . Combining the thus obtained deformation-energy landscapes with a simple Wentzel-Kramers-Brillouin (WKB) model [4],  $\alpha$ -decay properties, including  $Q$ -value and half-life, are obtained. Fission barrier heights are also derived from the potential-energy landscapes. Finally, the topography of the 4D deformation space is investigated in detail to search for most probable paths to fission, and their evolution with neutron and proton numbers across the Fm region. All along, comparison with experiment is made wherever measurements are available. A summary and conclusions are drawn in Sec. IV.

## II. THEORETICAL FRAMEWORK

### A. The Fourier shape parametrization

The description of the huge variety of shapes encountered all across the nuclear chart, from oblate

---

\*Electronic address: pomorski@kft.umcs.lublin.pl

deformations found in the transition region and corresponding to the progressive filling of the  $pf$  shell, to prolate shapes as realized in numerous rare-earth and actinide isotopes, requires a rich and flexible nuclear shape parametrization. The requirement is even more demanding for describing fissioning shapes, which are typically very elongated and necked-in. To model the physical reality as faithfully as possible (as far as that could be identified), it is desirable that the parametrization involves a large amount of deformation parameters, in order to take into account all of the degrees of freedom involved. For a numerical treatment, on the other hand, a very large number of deformation coordinates is prohibitive. The challenge therefore is to isolate the essential degrees of freedom and to describe these with a few physically relevant deformation parameters. Several shape parametrizations have been proposed, and are currently used for investigating the properties and decay of nuclei. The series expansion of the nuclear radius in spherical harmonics proposed by Lord Rayleigh [5] already in the 19th century, turned out to be able to describe a very rich variety of shapes, and is, till nowadays, one of the most widely used prescriptions in nuclear structure calculations. The achievement of this expansion strongly relies on the large amount of degrees of freedom taken into account. As soon, however, as elongated configurations are to be modeled, and most crucially for fissioning shapes, a nearly prohibitive number of deformation parameters is

required (as many as seven parameters were needed to describe the height of the fission barrier of  $^{232}\text{Th}$  when imposing a left-right symmetric mass split [6, 7]). Alternative parametrizations have been proposed since the days of Lord Rayleigh. Among the most powerful and popular ones we cite the quadratic surfaces of revolution (QSR) [8], the Cassini ovals [9, 10], the Funny-Hills (FH) shapes [11] and its modified version [12], as well as the expansion of the nuclear surface in a series of Legendre polynomials [13]. All these parametrizations are able to describe nuclear potential-energy landscapes rather well, and, in most cases, with a limited number of deformation degrees of freedom. For all of them, however, except those of Refs. [5, 13], they have the inconvenience that they do not allow to control their convergence. In what follows, we are going to use an innovative parametrization, initially introduced in Ref. [14], based on a Fourier expansion of the nuclear surface. This prescription has been shown [3] to be rapidly converging and to describe nuclear ground-state configurations, as well as very elongated and necked-in shapes, as they are encountered in the fission process close to scission with few deformation parameters only.

Within this Fourier parametrization [3, 14], we write, for axially symmetric shapes (a generalization to triaxial shapes will be given below), the distance  $\rho_s(z)$  from the symmetry axis of a surface point at coordinate  $z$  in cylindrical coordinates as

$$\frac{\rho_s^2(z)}{R_0^2} = \sum_{n=1}^{\infty} \left[ a_{2n} \cos\left(\frac{(2n-1)\pi}{2} \frac{z - z_{sh}}{z_0}\right) + a_{2n+1} \sin\left(\frac{2n\pi}{2} \frac{z - z_{sh}}{z_0}\right) \right] \quad (1)$$

where  $R_0$  is the radius of the corresponding spherical shape with the same volume. The extension of the shape along the symmetry axis is  $2z_0 = 2cR_0$  with left and right ends located at  $z_{\min} = z_{sh} - z_0$  and  $z_{\max} = z_{sh} + z_0$ , where  $\rho_s^2(z)$  vanishes, a condition which is automatically satisfied by Eq. (1). Here  $c = z_0/R_0$  is the Funny-Hills [11] elongation parameter ( $c < 1$  for oblate,  $c > 1$  for prolate shapes) which is related to the even Fourier coefficients by the volume-conservation relation:

$$\frac{\pi}{3c} = \sum_{n=1}^{\infty} (-1)^{n-1} \frac{a_{2n}}{2n-1}. \quad (2)$$

The shift coordinate  $z_{sh}$  in (1) is chosen such that the center of mass of the nuclear shape is located at the origin of the coordinate system. The parameters  $a_2$ ,  $a_3$ ,  $a_4$  describe, respectively, quadrupole, octupole and hexadecapole type deformations, which in the context of fission, are related to elongation, left-right asymmetry, and neck thickness, respectively.

Notice that our Fourier shape parametrization is, in a way, quite similar to the one due to Lord Rayleigh, in the sense that it is an expansion in a complete basis (trigonometric functions here, spherical harmonics there), but with the essential difference that, instead of the nuclear radius  $R(\theta, \varphi)$ , it is now the square of the distance  $\rho_s^2(z)$  of a surface point from the symmetry axis that is expanded in the basis functions. Such a description seems, indeed, to be better adapted to that kind of physical problem, as the success of the Funny-Hills [11, 12] or the Trentalange-Koonin-Sierk shapes [13] indicate.

As an example, a nuclear shape typically realized in the course of the fission process is displayed in Fig. 1. The various quantities discussed in the text are indicated in the figure.

To describe non-axial shapes, the cross section perpendicular to the symmetry axis is assumed to be of ellip-

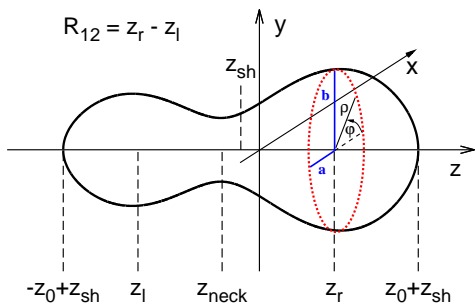


FIG. 1: (Color online) Schematic visualization, in cylindrical coordinates, of the parameters entering the definition of the profile function defined by Eq. (4). The quantities  $z_l$  and  $z_r$  localize the mass centers of left and right nascent fragment entering the definition of  $R_{12} = z_r - z_l$ .

soidal form, and defined by a non-axiality parameter

$$\eta = \frac{b - a}{b + a}, \quad (3)$$

which is the relative difference of the half axis  $a$  and  $b$  of the cross section perpendicular to the symmetry axis. Assuming that this parameter is the same all across the shape, the profile function can be written in cylindrical coordinates in the form

$$\rho_s^2(z, \varphi) = \rho_s^2(z) \frac{1 - \eta^2}{1 + \eta^2 + 2\eta \cos(2\varphi)}, \quad (4)$$

with  $\rho_s^2(z)$  given by Eq. (1).

The above defined shape parametrization is rapidly converging, even for fissioning shapes, as demonstrated in Fig. 2 of Ref. [3].

A somehow odd feature of the Fourier coefficients  $a_n$  which specify the shape, is their not necessarily transparent physical meaning. The Fourier coefficient  $a_2$ , for example, *decreases* with increasing elongation. To cure this inconvenience, we have introduced the following four new collective coordinates (see discussion in Ref. [3])

$$\begin{aligned} q_2 &= \frac{a_2^{(0)}}{a_2} - \frac{a_2}{a_2^{(0)}}, & q_3 &= a_3, \\ q_4 &= a_4 + \sqrt{\left(\frac{q_2}{9}\right)^2 + \left(a_4^{(0)}\right)^2}, \\ q_5 &= a_5 - (q_2 - 2)\frac{a_3}{10}, \\ q_6 &= a_6 - \sqrt{\left(\frac{q_2}{100}\right)^2 + \left(a_6^{(0)}\right)^2}, \end{aligned} \quad (5)$$

where the  $a_n^{(0)}$  are the values of the Fourier coefficients for the spherical shape. Note that the  $q_n$  coordinates

have been defined in such a way that they all vanish for a spherical shape. Their physical meaning is more transparent and intuitive when compared to that of the  $a_n$  coefficients. In the remainder of this work, we are therefore going to discuss the deformation properties of nuclei in a 4D deformation space made of the collective coordinates  $(\eta, q_2, q_3, q_4)$  which are directly related to non-axiality, elongation, octupole, and hexadecapole (neck-thickness) deformation. An alternative, but completely equivalent parametrization, based on an expansion of the deviation of the nuclear shape from a spheroid is proposed in Ref. [15].

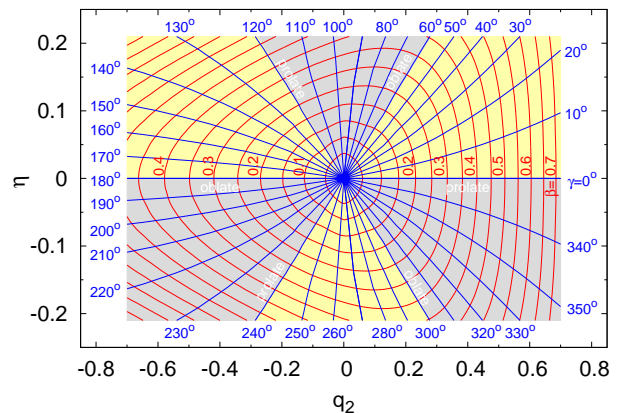


FIG. 2: (Color online) Visualization of the relation between the  $(\beta, \gamma)$  and the  $(q_2, \eta)$  deformation coordinates.

The connection between the here-proposed  $(q_2, \eta)$  coordinates and the generally used  $(\beta, \gamma)$  deformation parameters [16] is certainly worth to be discussed, in particular regarding the  $60^\circ$  symmetry of the latter. Let us recall that the  $(\beta, \gamma)$  variables are defined as

$$\beta = \frac{1}{X} \sqrt{Q_{20}^2 + Q_{22}^2} \quad \text{and} \quad \gamma = \arctan\left(\frac{Q_{22}}{Q_{20}}\right) \quad (6)$$

where  $Q_{20}^2$  and  $Q_{22}^2$  are the components of the mass quadrupole tensor

$$Q_{20} = \langle 2z^2 - r^2 \rangle, \quad Q_{22} = \langle y^2 - x^2 \rangle,$$

where  $X = 3r_0^2 A^{5/3} / \sqrt{5\pi}$  with the radius constant  $r_0$ .

The connection between the  $(\beta, \gamma)$  and the  $(q_2, \eta)$  coordinates is shown in Fig. 2, where the above mentioned  $60^\circ$  symmetry appears. This figure gives us the occasion to draw the attention of the reader to an inconvenience of both of these parametrizations at small deformation, and which calls for some cautious when interpreting the  $(\eta, q_2, q_3, q_4)$  deformation-energy landscapes. Due to the aforementioned symmetry, care has to be taken to avoid any “double-counting” of shapes. Let us take the example of an axially symmetric oblate shape defined by  $(q_2 = -0.35, \eta = 0)$  corresponding to a deformation of

( $\beta=0.25$ ,  $\gamma=180^\circ$ ). From Fig. 2 one concludes that the same shape is realized by ( $q_2 \approx +0.17$ ,  $\eta \approx 0.13$ ), equivalent to ( $\beta=0.25$ ,  $\gamma=60^\circ$ ). A similar correspondence can be established when considering prolate instead of oblate shapes. For example, the configuration ( $q_2=0.32$ ,  $\eta=0$ ) is defined equivalently by ( $\beta=0.30$ ,  $\gamma=0^\circ$ ), and due to the  $60^\circ$  symmetry, the latter defines the same shape as ( $q_2 \approx -0.19$ ,  $\eta \approx 0.13$ ) equivalent to ( $\beta=0.25$ ,  $\gamma=120^\circ$ ). We emphasize that, such a strict comparison can only be carried out for spheroidal-deformed shapes. When higher order multipolarities come into play, and importantly, at larger deformation, this picture is partially distorted.

Before closing the discussion on the relation between these two shape parametrizations, we notice that a constant value of  $\beta$  does *not* correspond to a constant elongation of the shape, as can be seen from Fig. 2. That is why we believe that, for investigating the possibility of triaxial shapes, the ( $q_2, \eta$ ) deformation space is better suited than the traditional ( $\beta, \gamma$ ) space.

As an illustration of the symmetry property of both these shape parametrizations, and the caution to be applied in the analysis of deformation-energy landscapes (calculated as described in the next subsection), let us consider the case of two deformations in the nuclei  $^{280}\text{Ds}$  and  $^{276}\text{Cn}$ . Different cross sections of the 4D deformation space are presented in Figs. 3 and 4. Each of these 2D landscapes has been realized by performing a minimization with respect to the other two deformation coordinates, unless specified otherwise.

The ( $q_2, q_3$ ) deformation-energy map of  $^{280}\text{Ds}$  in Fig. 3 shows two minima, one prolate ( $q_2 \approx +0.15$ ) and one oblate ( $q_2 \approx -0.15$ ). When investigating the ( $q_2, \eta$ ) cross section, one notices, however, that the apparently oblate minimum corresponds, in fact, to a triaxial solution ( $\eta \approx 0.05$ ). When looking again at Fig. 2, one concludes that a deformation ( $q_2 \approx -0.15$ ,  $\eta \approx 0.05$ ) characterizes the same shape as ( $q_2 \approx 0.1$ ,  $\eta \approx 0$ ) which is nothing but our prolate shape. In addition, the energy landscape in  $\eta$  direction is almost flat around the two minima. All this is a clear indication that this ‘‘oblate’’ minimum is nothing but the *mirroring* of the (true) prolate ground state, and does not correspond at all to a stationary point in the deformation-energy landscape that has anything to do with a true oblate deformation.

The situation is different for the case of the  $^{276}\text{Cn}$  nucleus illustrated in Fig. 4. Again two local minima are observed, one for a spherical shape ( $q_2=0$ ) and one for a prolate configuration ( $q_2 \approx +0.23$ ). When looking at the ( $q_2, \eta$ ) cross section, both solutions appear to be axially symmetric and are well separated in energy. This indicates a true shape coexistence with both local minima being left-right symmetric ( $q_3=0$ ) (middle and bottom rows of Fig. 4, left) and having slightly different hexadecapole deformation (middle and bottom rows of Fig. 4, right).

## B. The macroscopic-microscopic potential energy

The potential energy of a nuclear system is calculated in our approach within the macroscopic-microscopic model using the Lublin-Strasbourg Drop (LSD) [17] for the liquid-drop-type energy, including a curvature  $A^{1/3}$  term in the leptodermous expansion and a deformation dependent congruence energy term [18], which is well known to give a good description of nuclear ground-state masses and fission-barrier heights. The microscopic part is determined by the Strutinsky shell-correction energies [21] and pairing correlations [19] are derived in BCS theory with a seniority force and an approximate particle-number projection [22]. The single-particle energies and wave functions that enter such an approach are obtained as eigenvalues and eigenstates of a Yukawa-folded mean-field potential [23, 24] at given ( $\eta, q_2, q_3, q_4$ ) deformation. More details of the calculation are given in our previous work [3].

## III. RESULTS

Within the above-outlined theoretical framework, the 4D potential-energy landscapes of 324 even-even nuclei with charge numbers in the range  $92 \leq Z \leq 126$  and isospins  $40 \leq N - Z \leq 74$  are evaluated. The considered grid consists of 32 202 points in the ( $\eta, q_2, q_3, q_4$ ) space, with the following mesh:

$$\begin{aligned} \eta &= 0 \quad (0.03) \quad 0.12 \\ q_2 &= -0.45 \quad (0.05) \quad 2.35 \\ q_3 &= 0 \quad (0.03) \quad 0.21 \\ q_4 &= -0.21 \quad (0.03) \quad 0.21 \end{aligned}$$

The calculated landscapes are analyzed, looking for ground-state (and possible isomeric) equilibrium deformations, the corresponding  $\alpha$ -decay properties, fission barrier heights and the most probable fission paths in the region across Fm. The results of these investigations are reported in the following subsections.

### A. Equilibrium configurations

For each isotope, the ground-state equilibrium energy and shape were determined using the gradient oriented bisection method [25] and the Gauss-Hermite approximation [26]. A so-determined equilibrium configuration is characterized by the collective coordinates ( $\eta^{eq}, q_2^{eq}, q_3^{eq}, q_4^{eq}$ ) the values of which are displayed as a function of  $Z$  and  $N - Z$  in Fig. 5.

The top part of Fig. 5 shows that most of the systems considered in this work are axially symmetric ( $\eta^{eq} \approx 0$ ). A few exceptions are noteworthy to discuss, though. First, one observes two somehow isolated cases: the element Ds ( $Z = 110$ ) which, in particular for  $A \approx 270$ ,

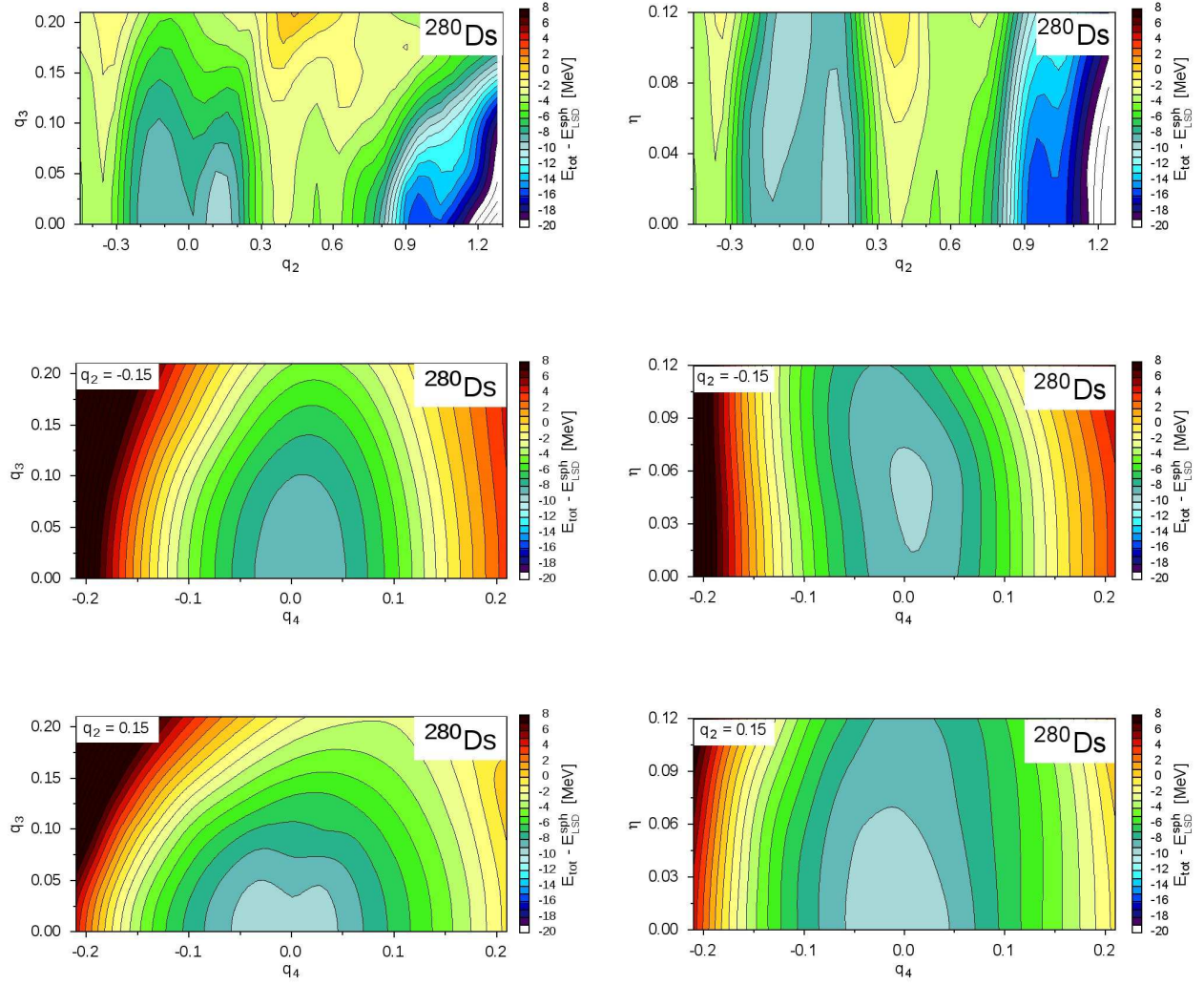


FIG. 3: (Color online) Deformation energy of  $^{280}\text{Ds}$  on the  $(q_2, q_3)$  plane for  $\eta = 0$  minimized with respect to  $q_4$  (top left) and on the  $(q_2, \eta)$  plane minimized with respect to  $q_3$  and  $q_4$  (top right). The  $(q_4, q_3)$  and  $(q_4, \eta)$  cross sections around the oblate and prolate minima are shown in the middle and bottom row, respectively.

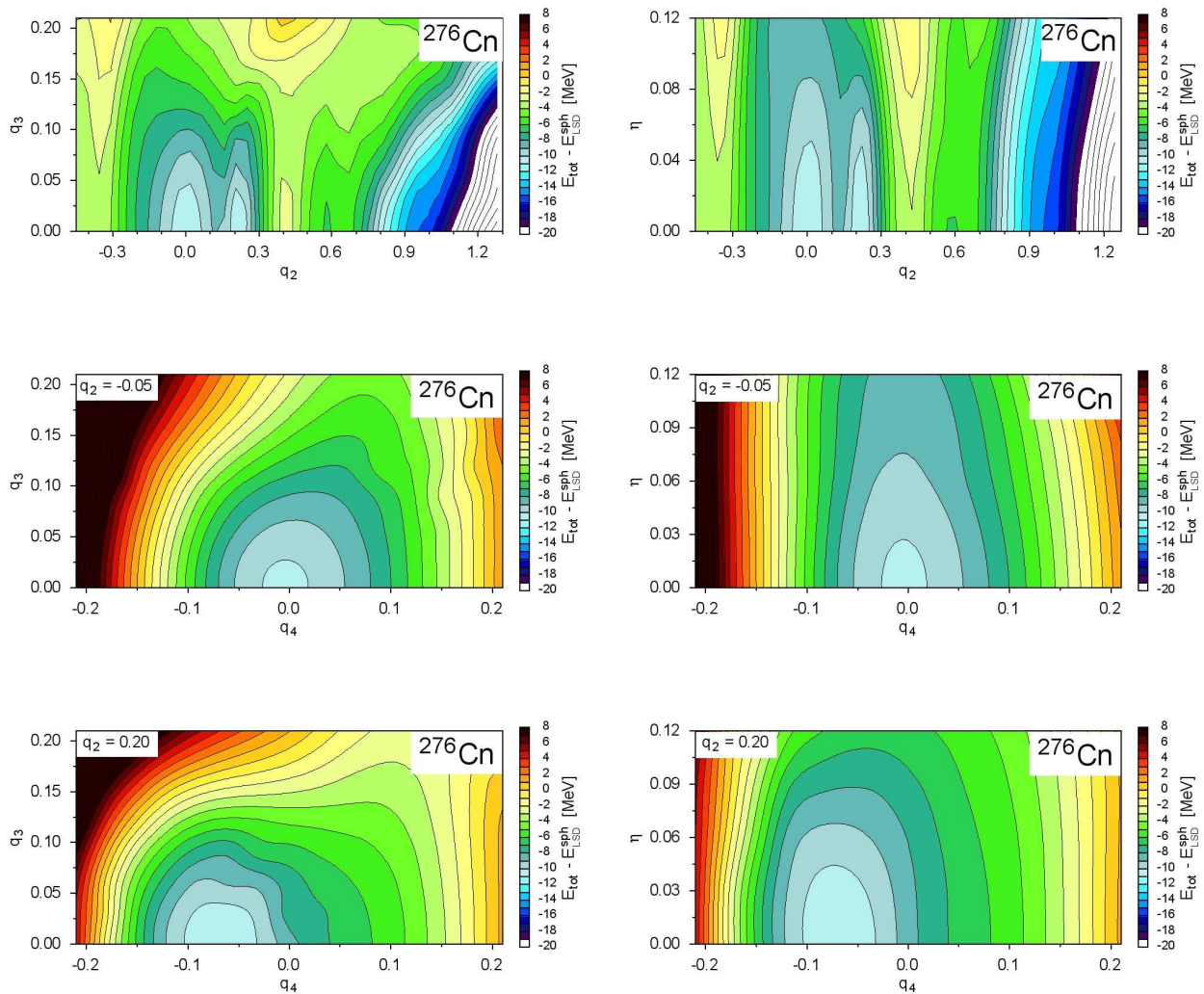


FIG. 4: (Color online) Same as in Fig. 3 but for  $^{276}\text{Cn}$ .

seems to be triaxial, as well as  $^{292}\text{Og}$  ( $Z=118, N=174$ ). At first sight, the nuclear system ( $Z=120, N=166$ ) seems to possess a quite strong non-axiality. Having, however, a closer look at its quadrupole parameter  $q_2$  (second panel in Fig. 5), one notices that this parameter turns out to be almost vanishing, and, as we have explained before, near the spherical shape, the non-axiality degree of freedom loses its meaning. In addition one observes, for  $102 \leq Z \leq 110$ , a diagonal downward-sloping band running over the isospin interval  $64 \leq N - Z \leq 72$ . The corresponding isotopes (from  $^{276}\text{No}$  to  $^{284}\text{Ds}$ ) are predicted to possess a slight triaxiality, and/or to be soft with respect to triaxial deformations. It is interesting to notice that all nuclei in this band have a neutron number  $N$  around 174. As we will see in the next subsection, these nuclei are prolate-deformed. Hence, the present model predicts a triaxial "window" across  $N \approx 174$  for elements from No to Ds. We nevertheless emphasize that a value of  $\eta \approx 0.07$  corresponds to a non-axial

deformation where the longer of the two half axis is only 15% larger than the shorter one. That is to say that the observed effect is small. Please also note that for Fl ( $Z=114$ ) isotopes with isospin  $N - Z$  values between 54 and 62, for which a non-zero  $\eta^{\text{eq}}$  value is deduced from the top part of Fig. 5, have a practically vanishing  $q_2^{\text{eq}}$  value (second panel), and are therefore close to a spherical shape where the non-axiality parameters  $\eta$  and  $\gamma$  lose their meaning. The observation about a dominating axial symmetry in the region, and the occurrence of a weakly triaxial "window" around  $N \approx 174$  for No to Ds is consistent with predictions by other models, like e.g. the self-consistent approaches of Ref. [27, 28].

Equilibrium quadrupole-type deformations are investigated in the second panel of Fig. 5. Transuranic elements with masses below  $A \approx 280$  are observed to possess a prolate ground-state deformation, while beyond  $A \approx 300$  an oblate configuration is predicted, especially in the vicinity of the nucleus  $^{304}122$ . It is interesting to note

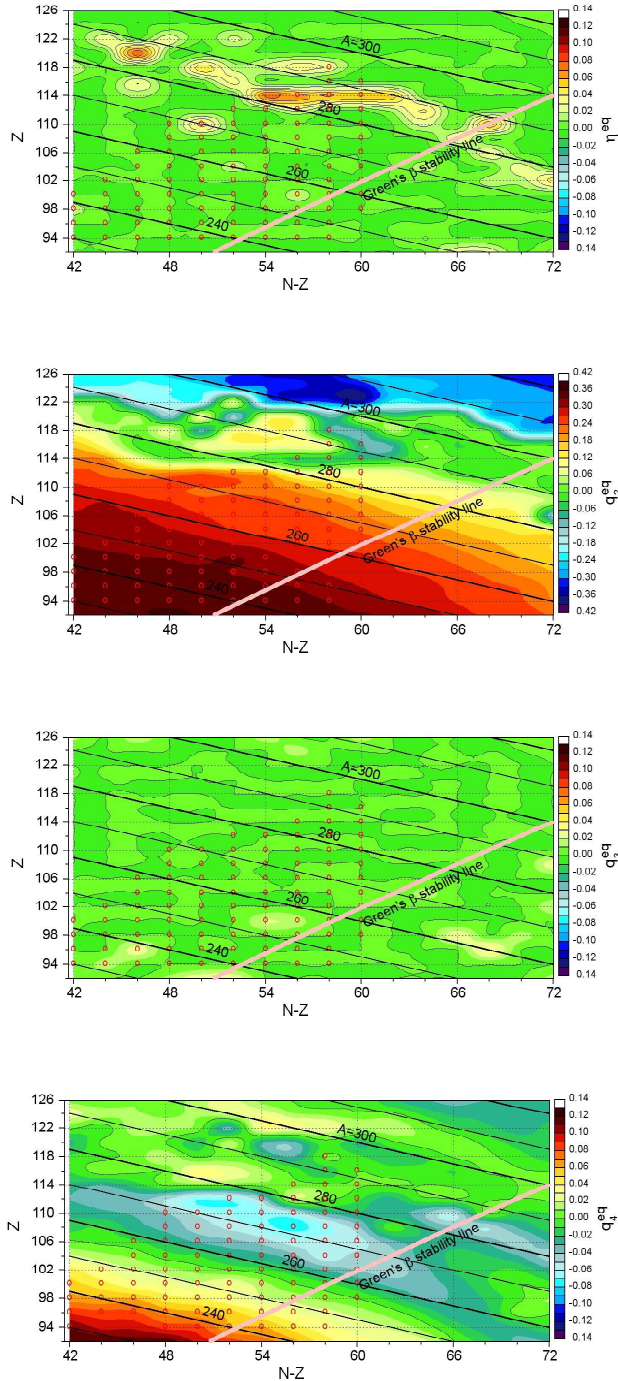


FIG. 5: (Color online) Values of the collective coordinates ( $\eta^{eq}$ ,  $q_2^{eq}$ ,  $q_3^{eq}$ ,  $q_4^{eq}$ ) (from top to bottom) at equilibrium deformation defined as the ground-state minimal-energy configuration on the  $(N - Z, Z)$  plane. The circles denote already discovered isotopes and the thick (pink) line shows the  $\beta$ -stable nuclei. The thin (black) lines correspond to the constant mass number  $A$ .

that, up to around  $Z = 114$  the magnitude of the prolate

elongation steadily decreases for all elements with increasing  $N$  (or equivalently  $N - Z$ ). For heavier elements the dependence on  $N$  is more erratic. These different trends depending on  $Z$  are very likely to be connected to the evolution of shell corrections with  $Z$  and  $N$ , as further discussed below. A similar trend for quadrupole deformation across the region was anticipated both with macroscopic-microscopic and self-consistent methods (see e.g. Refs. [27, 29, 30]).

Left-right asymmetric shapes are investigated in the third panel of Fig. 5. One concludes that the ground-state is expected to be essentially left-right symmetric ( $q_3^{eq} \approx 0$ ) for all nuclei in the region.

Finally, the last panel of Fig. 5 suggests that, while the lighter actinides with  $A \approx 230$  have a substantial hexadecapole ground-state deformation ( $q_4^{eq} \approx +0.10$ ), corresponding to a diamond-like (rugby-ball type) configuration, those in the region between Hs and Cn with  $A \approx 270$  are predicted to have strong negative hexadecapole deformation ( $q_4^{eq} \approx -0.08$ ), looking a bit like a rounded-off rod. Again, one notes a rather steady evolution with  $N$  for elements up to  $Z \approx 108$ , and presumably structural effects for higher  $Z$ 's.

Since the macroscopic energy has no minimum for SHE isotopes, the equilibrium configuration is governed by shell effects. The microscopic contribution defined as the total potential energy at equilibrium relative to the macroscopic energy at spherical shape,  $\delta E_{mic}^{eq} = E_{tot}^{eq} - E_{LSD}^{sph}$ , is shown in Fig. 6, as in Fig. 5, on the  $(N - Z, Z)$  plane. Two regions of strong microscopic effects are visible. The island centered around  $Z = 108$ ,  $N - Z = 54$  is driven by the deformed  $N = 162$  shell; large prolate deformation can, indeed, be deduced from the second panel of Fig. 5. The evidence for stabilization through deformation in the  $^{270}\text{Hs}$  region was experimentally confirmed [31]. Our calculations predict even stronger microscopic effects in a band running from  $Z \approx 114$  to  $Z \approx 118$  and with  $48 \leq N - Z \leq 66$ . The effect is largest at  $Z = 116$  for the  $^{286}\text{Lv}$  and  $^{290}\text{Lv}$  isotopes, corresponding to  $N = 170$  and  $174$ . Figure 5 shows that nuclei in this band are characterized by a weak prolate deformation. The present model therefore predicts that the next ‘‘magic configuration’’ (not yet reached by the experiment) would be slightly prolate-deformed and located at  $Z = 114 - 116$  and  $N = 170 - 174$ . A separate analysis of the proton and neutron microscopic corrections shows that this stabilization is mainly driven by the neutrons in our calculations. No evidence for spherical magicity at  $Z = 114$  and  $N = 184$  is apparently seen in our results, contrary to what was anticipated in other macroscopic-microscopic models [33–35].

While Fig. 6 gives a condensed overview for the nuclei in the whole region, a more detailed quantitative visualization is proposed in Fig. 7. There, the evolution of the quantal corrections to the ground-state energy is shown separately for each isotopic chain, being displayed

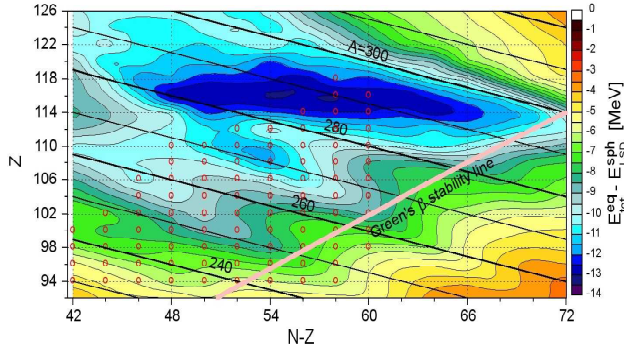


FIG. 6: (Color online) Ground-state microscopic contribution to the potential energy for the nuclei of Fig. 5.

for all  $Z$  values included in the 2D overview of Fig. 6 as function of the neutron number. The shell-stabilized configurations discussed above appear as local, more or less abrupt, dips. The deformed shell effect at  $N = 162$  that develops from U towards Hs, and vanishes beyond Cn, is clearly seen. Although of weaker magnitude, a similar shell effect becomes visible at  $N = 152$  for elements between Cm and Sg, which is also corroborated by experimental observation [31]. The  $N = 152$  deformed region is located in Fig. 6 “southwest” of the  $N = 162$  island. Finally, the new predicted “SHE magic shell closure” discussed above first appears as a dip at  $N = 174$ , starting from say Ds. For heavier elements, the deformed  $N = 162$  and  $N = 174$  shells merge, producing the wide band of strong stabilization discussed previously from  $Z \approx 114$  to  $Z \approx 118$  and with  $168 \leq N \leq 178$ .

The presentation adopted in Figs. 5 and 6 confers a fast overview of the ground-state properties across the entire studied region. It is the result of the analysis of the theoretical 4D potential-energy landscapes. To illustrate the richness of these landscapes in more detail, their progressive evolution with proton and neutron numbers, and the possible occurrence of metastable, isomeric states, 2D cross sections of the 4D deformation space are presented in Fig. 8. The deformation energy, defined as the total potential energy relative to the spherical liquid-drop energy, is displayed for three isotopes of the Rf, Sg and Hs elements, in the  $(q_2, \eta)$  (top part of the figure) and  $(q_2, q_3)$  (bottom part of the figure) subspaces. Each of the 2D surfaces is obtained, as already mentioned above, after minimization with respect to the two remaining collective variables. The selected isotopes for a given  $Z$  are characterized by the same values of the isospin  $N - Z = 52, 54$  and  $56$ . The corresponding  $N$  values vary between 156 and 164. From the  $(q_2, q_3)$  landscapes, all these nuclei are found to have a prolate ground-state deformation with  $q_2 \approx 0.28$ , and to be left-right symmetric ( $q_3 = 0$ ). The analysis of the

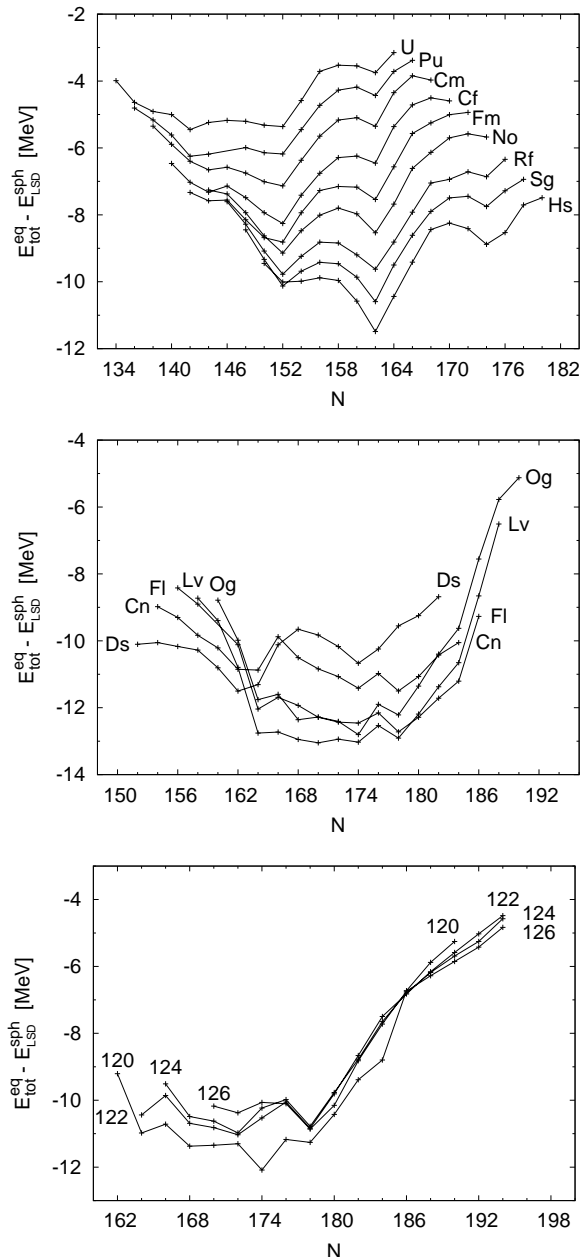


FIG. 7: (Color online) Ground-state microscopic contribution to the potential energy along isotopic chains between U and Hs (top), between Ds and Og (middle), and between elements  $Z = 120$  and  $Z = 126$  (bottom).

$(q_2, \eta)$  landscapes further confirms the axial symmetry of these isotopes.

It is interesting to observe in Fig. 8 (not visible in Fig. 5), that there is a left-right symmetric shape-isomeric state which appears for the Rf isotopes at  $q_2 \approx 0.8$ , and, though less pronounced, for Sg and Hs at  $q_2 \approx 0.6$ . The occurrence of the isomeric local minimum is seen to strongly depend on *both*  $N$  and  $Z$ . Further, for the selected isotopes having the same  $N - Z$ , the observed evolution implies that the appearance of this state is not



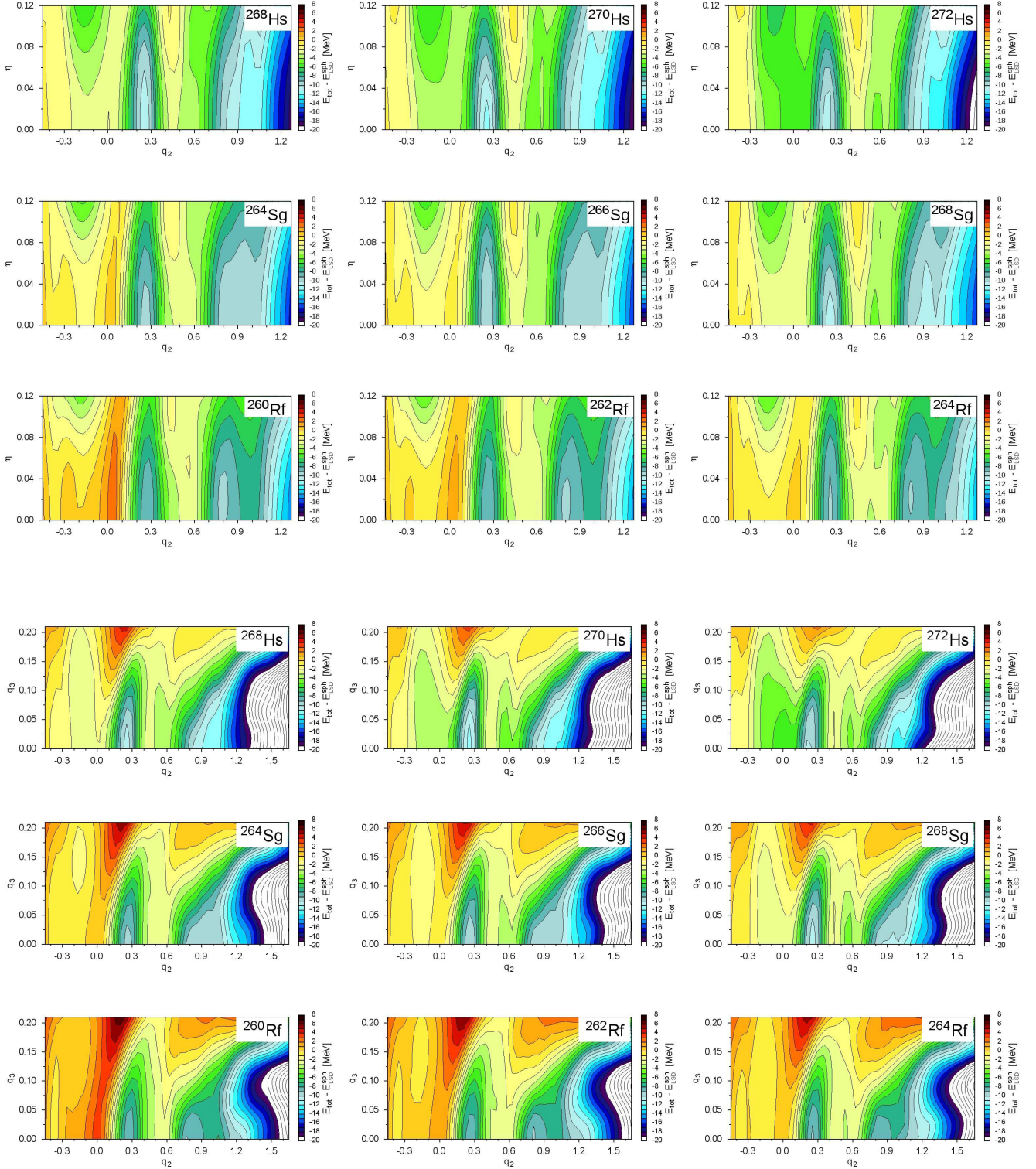


FIG. 8: (Color online) Deformation energy in the  $(q_2, \eta)$  (upper half) and  $(q_2, q_3)$  (lower half) sub-spaces for three isotopes of Hs (first row), Sg (second row) and Rf (third row). Each column corresponds to a specific  $N - Z$  value: 52 (left), 54 (middle) and 56 (right).

governed by  $N - Z$  either. Altogether the appearance of this isomeric state suggests that it originates from the subtle interplay of neutron and proton microscopic effects at large deformation.

## B. Alpha-decay properties

Alpha radioactivity is the dominant decay mode in the VHE and SHE region. Most of the currently known heaviest nuclei have actually been identified due to their connection via  $\alpha$ -decay (see [36] and Refs. therein) to their previously known daughter nucleus. The availability of reliable  $Q_\alpha$  predictions is therefore crucial for an assignment of new elements. The energy released when the nucleus emits an  $\alpha$  particle is directly related to the nuclear masses. Hence,  $Q_\alpha$  values are also an indirect way to test nuclear-mass models. The macroscopic-microscopic model used in the present work has shown to provide a particularly good description of nuclear masses [17]. Reliable predictions for  $Q_\alpha$  values are therefore anticipated.

The calculated  $Q_\alpha$  are displayed in Fig. 9 as function of the mass number for different isotopic chains from Pu up to element  $Z = 124$ . The aforementioned  $N = 162$  deformed shell appears as a dip at the corresponding mass for elements between Fm and Ds. Similarly, a local minimum is predicted, due to some kind of shell closure in the Sg, Hs, Ds and Cn isotopic chains, at  $N \approx 174$ . To explain the change of magic numbers from  $N = 162$  to  $N = 174$ , please notice that it is precisely in this mass region, when going from  $A \approx 270$  to  $A \approx 290$ , that the ground-state deformation changes from strongly prolate to close to spherical, as can be seen on the second panel of Fig. 5. The weak microscopic effect at  $N = 152$  appears as a very shallow minimum beyond Cm up to Sg. One notices the absence of a clear and systematic local minimum at  $N = 184$ , in contrast to the predictions of other models (see e.g. Ref. [33]). A comparison of the results of our calculations with the experiment [37], wherever available, is observed to be very good. The apparently good description of nuclei, as function of  $Z$ , at and around  $N = 152$  and  $162$ , is particularly noteworthy.

Encouraged by the promising results of our model for  $Q_\alpha$  energies, we compute the  $\alpha$ -decay half-life  $T_{1/2}^\alpha$  (for which  $Q_\alpha$  is the main ingredient) in the framework of the Gamow-type WKB approach of Ref. [4], with no additional adjustment of any parameter. The corresponding results are presented in Fig. 10. In addition to the experimental half-lives, two types of theoretical estimates are displayed there. Open black circles correspond to the  $Q_\alpha$  energies produced by our macroscopic-microscopic model, while full blue circles are obtained with the experimental  $Q_\alpha$  values where available. These last estimates are found to agree almost perfectly with the experimental data [38], which, to our understanding, is a clear indication of the value of our Gamow-type WKB approach.

The difference between the two theoretical curves demonstrates the strong sensitivity of  $T_{1/2}^\alpha$  on the precise value of  $Q_\alpha$ . Similar to the case of  $\alpha$ -decay energies, shell effects lead to local minima in the evolution of  $T_{1/2}^\alpha$  with mass number  $A$ .

## C. Fission barriers

Besides  $\alpha$ -decay many VHE and SHE isotopes are characterized by a high probability of decaying via spontaneous fission [39]. Accurate quantitative predictions of spontaneous fission properties remain a challenge for theory, due to the poor knowledge of the many ingredients entering its description (see [40] and Refs. therein). Improving our understanding of the process is important even for areas outside traditional nuclear physics, like astrophysics [41].

To address the question of stability against spontaneous fission, the fission barrier constitutes a crucial quantity. Its heights derived from the 4D landscapes calculated in our approach are displayed in Fig. 11 as function of  $N - Z$  and  $Z$ . One notices a rather high fission barrier in the region centered around  $^{270}\text{Hs}$  ( $V_B \approx 9$  MeV), but also around  $^{252}\text{Fm}$  ( $V_B \approx 8$  MeV). These islands of higher stability against spontaneous fission are related to the  $N = 162$  and  $N = 152$  shell effect, respectively. Large barriers ( $V_B \approx 8$  MeV) are also predicted near  $^{278}\text{Fl}$  ( $N = 164$ ). These should lead to increased stability against fission of the corresponding isotopes.

Our estimates on fission barriers are consistent both qualitatively and quantitatively with the predictions by the macroscopic-microscopic model of Moller et al. [34, 35] in Hs and Fm isotopes. Similarly to Moller, we again observe enhanced fission-barrier heights in a band ( $Z = 114 - 118$ ,  $N - Z = 48 - 66$ ), even though the effect seems somehow weaker in our approach as compared to his. Still slightly different predictions are published in e.g. Refs. [42–44].

Figure 11 displays our calculated barrier heights as function of mass number  $A$  for the same isotopic chains as in Figs. 9 and 10. Comparison with the (unfortunately sparse) experimental data [45–48] shows that our estimates are, indeed, very reasonable.

In recent works [49, 50] we have also applied the above-quoted simple WKB approach to estimate the spontaneous fission half-lives. Comparison with experiment between Th and Fl is presented in Fig. 10 of Ref. [49]. The description by our model is impressively good, with deviations from the experimental data which are on the average less than one order of magnitude what is remarkable in the field (see e.g. discussion in Ref. [40]).

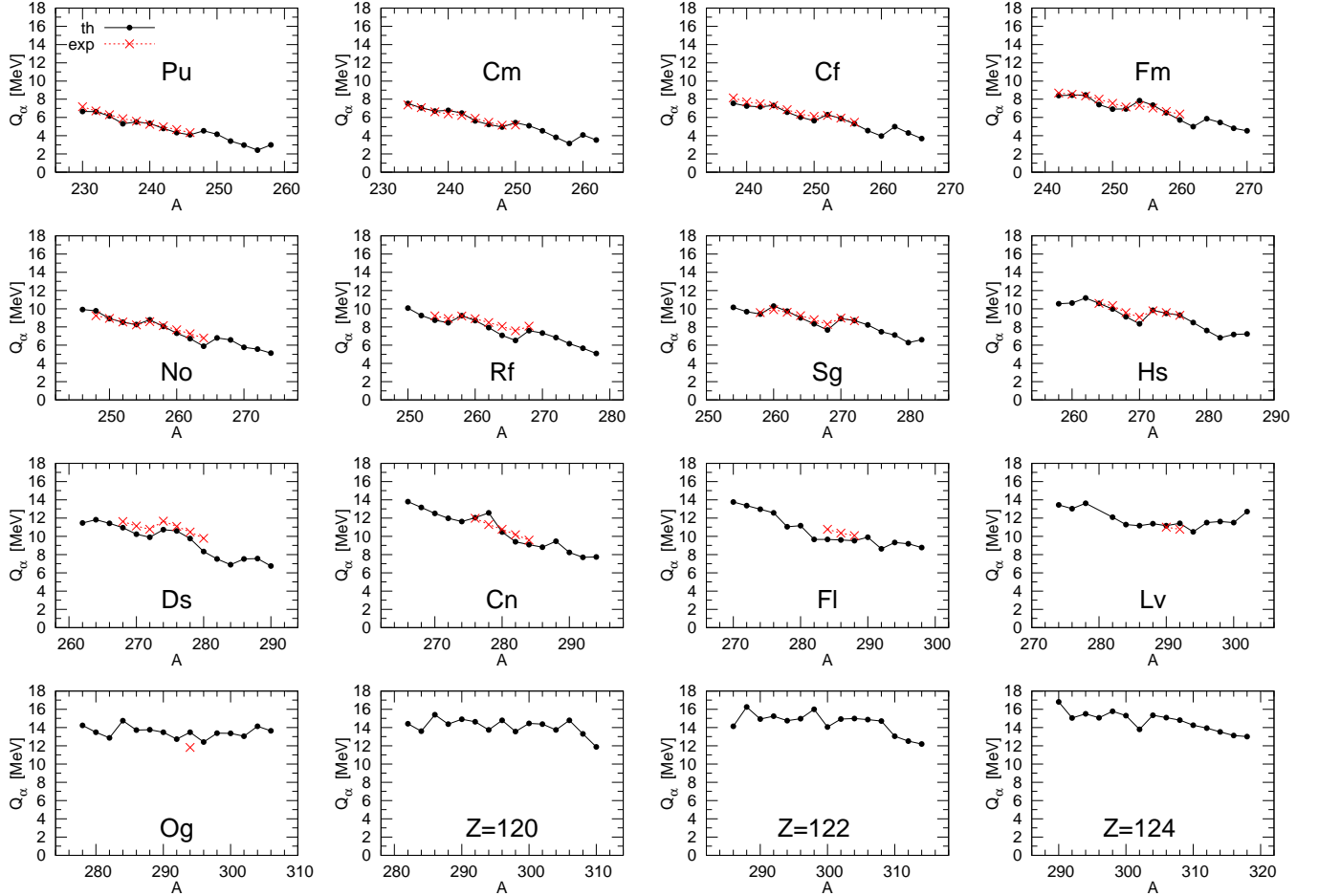


FIG. 9: (Color online) Calculated  $Q_\alpha$  energies for different isotopic chains compared to the experimental data (red crosses) [37] where available.

#### D. Fission valleys and fission modes

Fission-fragment properties (mass, charge, and kinetic-energy distributions) are determined by the evolution of the fissioning system on the multidimensional deformation-energy landscape. This path, between the initially compact configuration up to the scission into two separate fragments, is influenced by both static and dynamical effects, with the former effects presumably dominating at low excitation energy. High quality calculations of the potential-energy landscape are therefore essential for reliable predictions on fragment properties. Conversely, measured fragment properties, and at first place, their mass distributions, constitute a unique tool for probing the potential-energy landscape, and thereby testing the underlying model.

It is an experimentally well-established fact that the fission-fragment mass distribution in low-energy fission of actinides around U is asymmetric (see [51] and Refs. therein). On the theoretical side, there is also general agreement that this asymmetry originates from the influence of shell effects in the nascent fragments

[52, 53]. A further analysis of the correlation between mass and kinetic energy reveals the presence of different fission channels or modes [54, 55]. Dominant fission modes are attributed to the influence of shell effects in the nascent *heavy* fission fragment, one channel near the doubly magic  $^{132}\text{Sn}$ , and another at a deformed shell closure around neutron number  $N=88$ . The competition between these two modes and the additional symmetric mode depends on the fissioning nucleus [56, 57]. The sharp transition from asymmetric to symmetric fission which was experimentally observed between  $^{256}\text{Fm}$  and  $^{258}\text{Fm}$  [58], with a very narrow mass distribution and high kinetic energy, was interpreted as the signature of the formation of two close-to-magic Sn isotopes in a compact scission configuration [59]. In other words, with increasing mass of the fissioning system, the light-mass peak in actinide fission approaches the heavy one. The same feature was observed for several isotopes of other elements slightly beyond Fm [39, 58–61].

The experimental findings in the Fm region triggered a very intense theoretical effort, with both macroscopic-microscopic and self-consistent models in

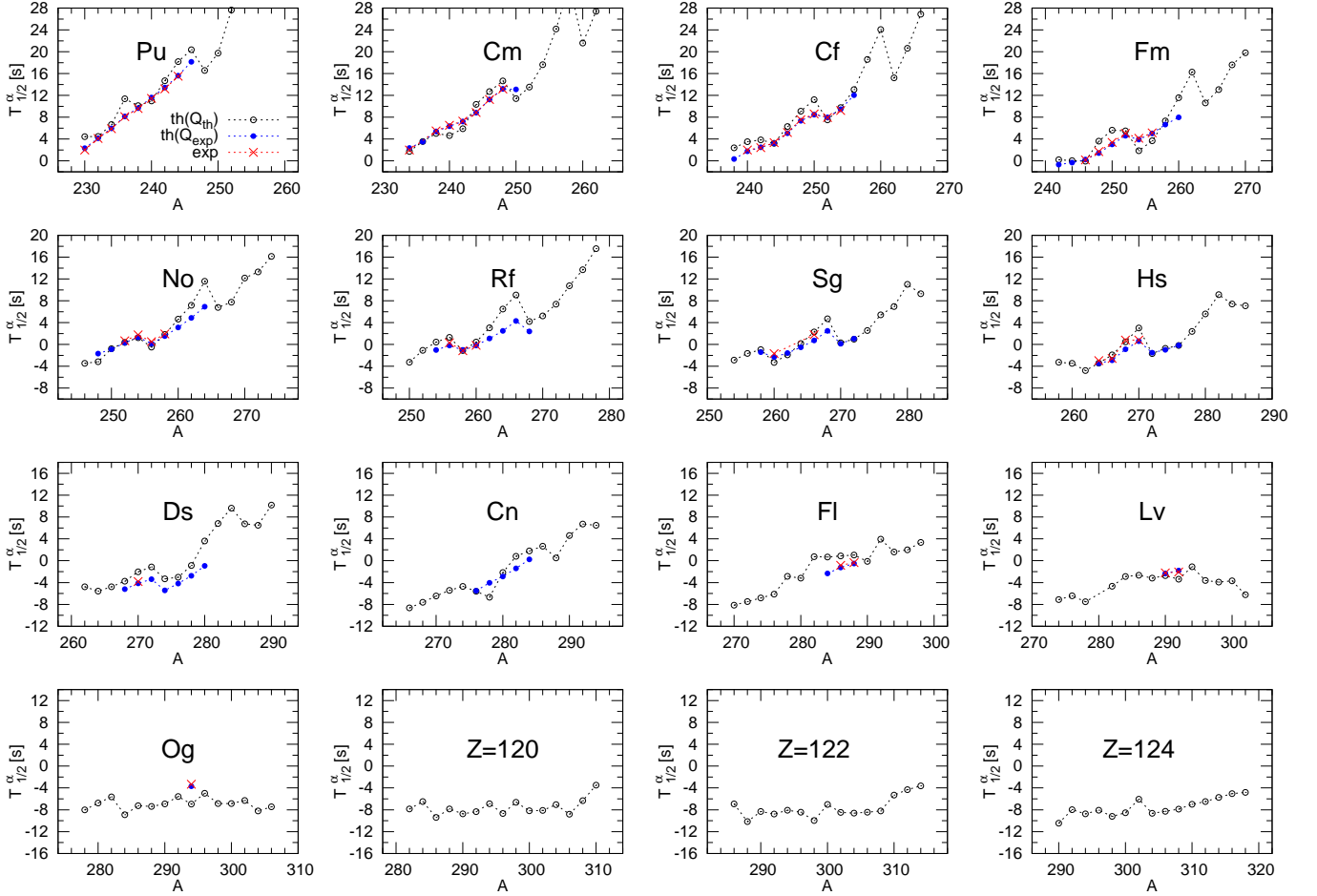


FIG. 10: (Color online) Calculated  $T_{1/2}^{\alpha}$   $\alpha$ -decay half-lives for different isotopic chains compared to the experimental data (red crosses) [38] where available. Two theoretical estimates given by the open black and full blue circles are shown (see the text).

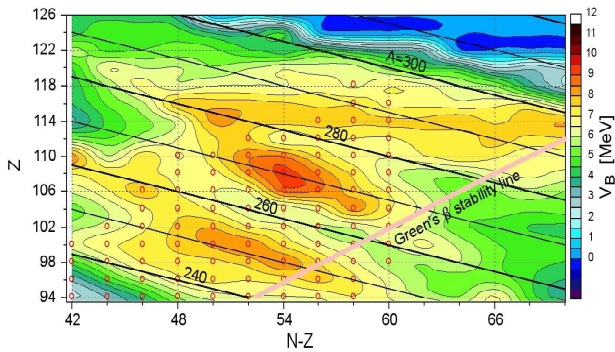


FIG. 11: (Color online) Fission barrier height for the considered nuclei as function of  $Z$  and  $N - Z$ .

order to identify the origin behind this particular fission mechanism (see e.g. Refs. [62–68]). In our previous

work [3] we analyzed the 4D potential-energy landscapes computed within the present approach for a wide range of pre-actinides and actinides. Although only qualitative at this level <sup>1</sup>, the study showed that our model provides a consistent description of the competition and evolution of asymmetric and symmetric fission up to Pu. Motivated by this encouraging result, we propose in the present work to extend the study to heavier elements. It is in particular interesting to investigate whether the 4D deformation space based on the Fourier shape parametrization is able to account for the specific modes which lead to the abrupt transition observed in the Fm region. The method used to identify fission valleys in the 4D landscape was detailed in Ref. [3]. In short, we identify

<sup>1</sup> A more quantitative estimate of the fragment mass distribution would require dynamical calculations. Static arguments based on the sole potential-energy landscape remain qualitative, even though, in low-energy fission, the potential-energy topography allows already for a faithful estimate of the shape of the distribution.

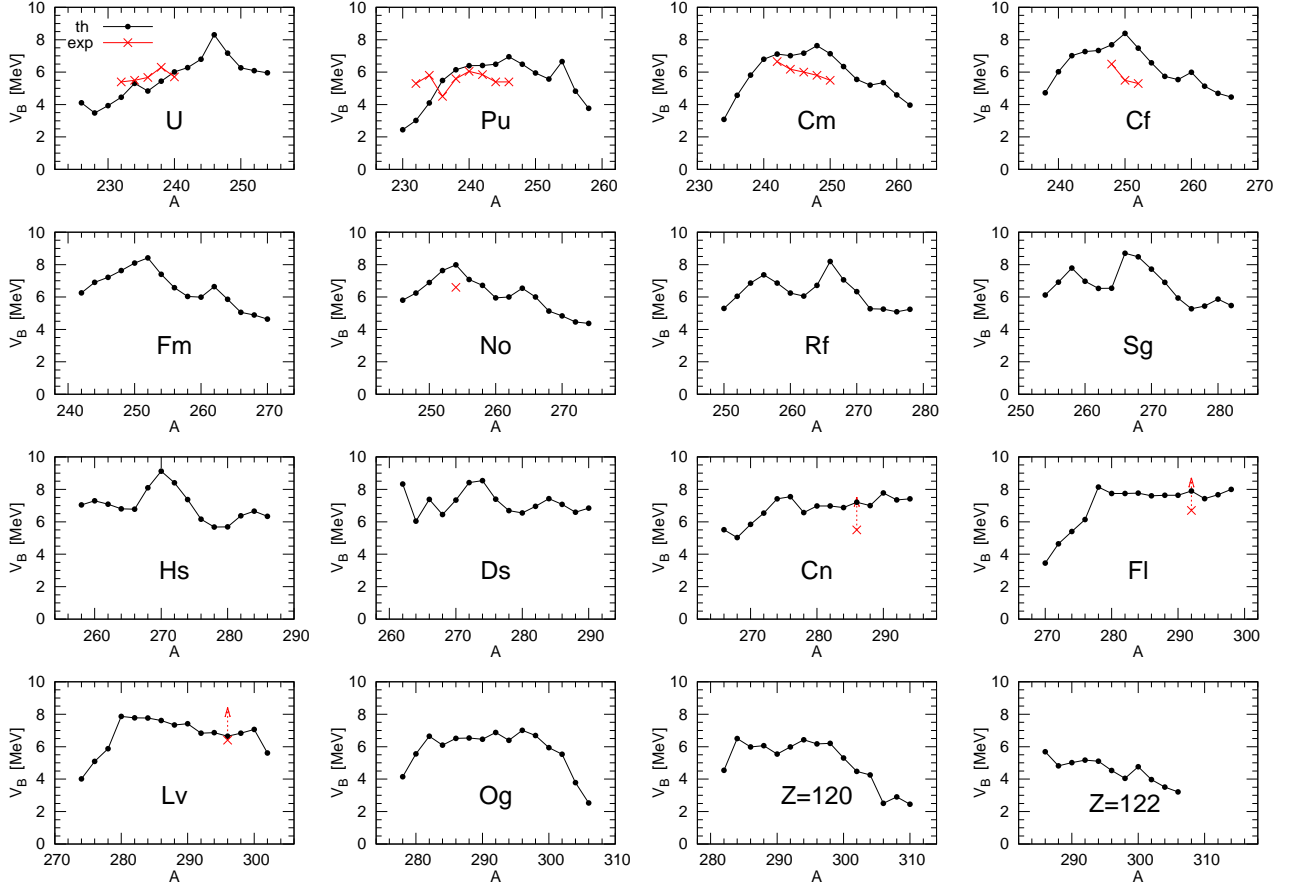


FIG. 12: (Color online) Similar to Figs. 9 and 10 for calculated fission-barrier heights compared to the data [45–48].

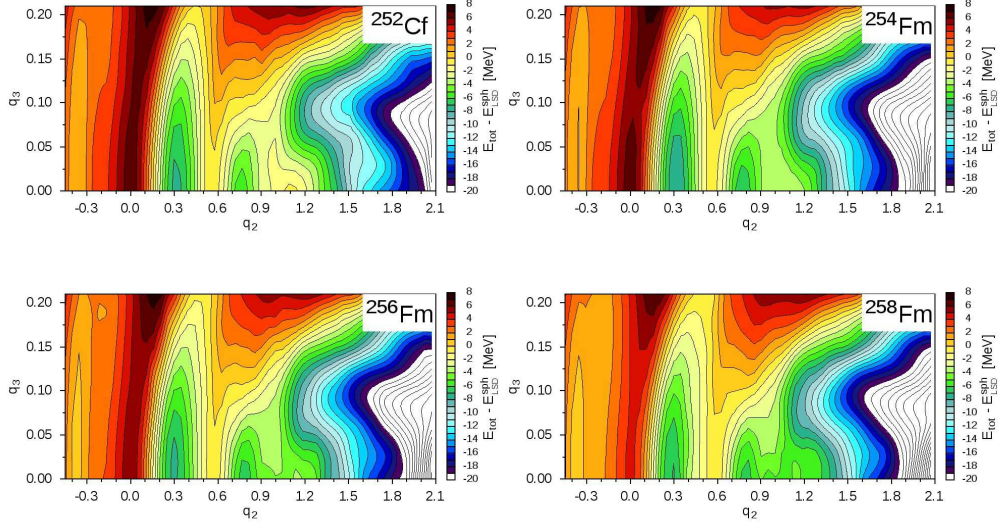


FIG. 13: (Color online) Deformation energy in the  $(q_2, q_3)$  plane minimized with respect to  $\eta$  and  $q_4$ , for  $^{252}\text{Cf}$  and  $^{254-258}\text{Fm}$ .

as a fission valley a continuous path, running through the 4D space, with the criterion of slowly varying values along each of the collective coordinates. As a first step, we search for paths to fission in the  $(q_2, q_3)$  potential-energy map obtained after minimization with

respect to  $\eta$  and  $q_4$ . Then, along each “candidate path” (or valley), step by step in  $q_2$ , we look whether it is associated with a continuous set of minima in the other 2D spaces, like  $(\eta, q_2)$ ,  $(q_2, q_4)$ ,  $(q_3, q_4)$ , etc.

The  $(q_2, q_3)$  potential-energy maps for  $^{252}\text{Cf}$  and

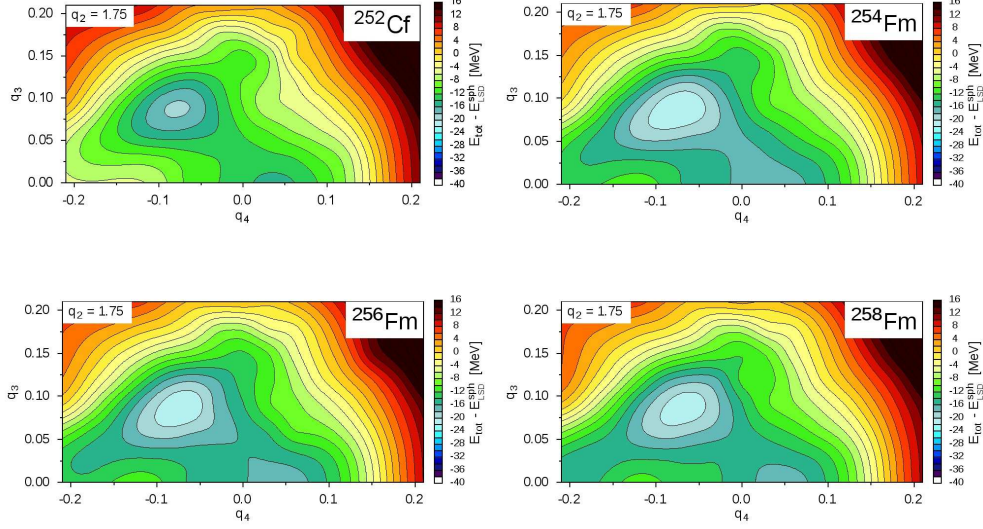


FIG. 14: (Color online) Deformation energy in the  $(q_4, q_3)$  plane for  $q_2 = 1.75$ , for  $^{252}\text{Cf}$  and  $^{254-258}\text{Fm}$ .

$^{254-258}\text{Fm}$  are displayed in Fig. 13. For all these nuclei, one observes a prolate-deformed ground-state minimum at  $q_2 \approx 0.3$  and an isomeric minimum at  $q_2 \approx 0.8$ . For  $^{252}\text{Cf}$  the topography of the landscape resembles that of lighter actinides (see e.g. the case of  $^{228}\text{Ra}$  in Fig. 8 of Ref. [3]), although some structures at and beyond the outer saddle ( $q_2 \approx 1.1$ ) are somewhat less pronounced. The maximum at the outer saddle being located around  $q_3 = 0$ , the  $(q_2, q_3)$  landscape suggests that  $^{252}\text{Cf}$  will predominantly fission asymmetrically at low excitation energy. This is confirmed by the  $(q_3, q_4)$  maps analyzed for successive  $q_2$  along the path to scission. In Fig. 14 (upper left) we show the map of  $^{252}\text{Cf}$  at  $q_2 = 1.75$ . The latter value was selected corresponding to an elongation beyond the outer-saddle region, where the descent to scission is already initiated. The choice is somehow arbitrary, but since the fission valley runs nearly parallel to the  $q_2$  axis once the descent is initiated (see Fig. 13), the location in  $q_3$  (equivalently, mass asymmetry) of the actual scission does not depend strongly on this precise choice of  $q_2$ . As noted previously, the left-right asymmetry of the valley is determined rather early, slightly beyond the outer saddle [52]. The  $(q_4, q_3)$  map shows two minima, one at  $(q_3 \approx 0.07, q_4 \approx -0.075)$  and the other at  $(q_3 \approx 0.0, q_4 \approx 0.03)$ , corresponding respectively to asymmetric and symmetric mass splits, with compact and elongated scission configurations [3]. The former minimum is much deeper, suggesting the dominance of mass-asymmetric fission, with a location in  $q_3$  corresponding to a heavy fragment mass around 140, consistent with experiment [69]. Comparing this result in particular with Fig. 8 of Ref. [3] one concludes that the pattern and location of the fission valleys in the 4D landscape for  $^{252}\text{Cf}$  are similar to those obtained for the lighter actinides.

Moving to the Fm isotopes, a close inspection of

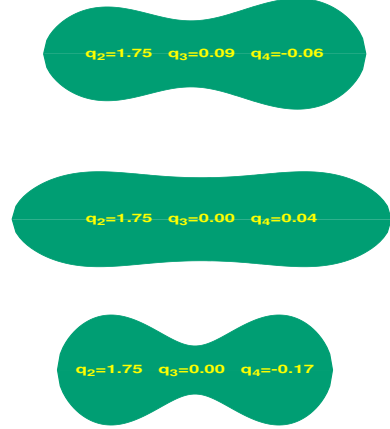


FIG. 15: (Color online) Nuclear shape for three different sets of collective variables  $(q_2, q_3, q_4)$ .

Fig. 13 suggests a progressive departure from the above trend with increasing Fm mass. For  $^{254}\text{Fm}$  the potential-energy landscape in the outer-saddle region ( $q_2 \approx 1.1$ ) is rather flat in  $q_3$  direction with the absence of a maximum centered at  $q_3 = 0$  as this was the case for  $^{252}\text{Cf}$ . For heavier Fm isotopes, the potential energy even decreases towards symmetry. In other words, there is a progressive migration of the lowest outer-saddle point from  $(q_3 \approx 0.07)$  to  $(q_3 \approx 0.0)$  between  $^{254}\text{Fm}$  and  $^{258}\text{Fm}$ , suggesting the emergence of a favored symmetric splitting. This preference of equal-mass partition increases further for still heavier Fm isotopes (not shown). In order to get a deeper insight into

the reason for this migration, let us consider the  $(q_3, q_4)$  maps for  $q_2 = 1.75$  in Fig. 14. For all three Fm isotopes, one notices the presence of the same minima as for  $^{252}\text{Cf}$ , identified as the compact asymmetric and elongated symmetric (so-called super-long) modes. However, with increasing Fm mass, a *third* distinct minimum starts to develop, localized at  $q_3 = 0$  and  $q_4$  in the range  $-0.2$  to  $-0.15$ , suggesting a second mode of symmetric fission. The profiles of the nuclear shapes corresponding to the three minima identified in Fig. 14 are displayed in Fig. 15. The two minima, common to Cf and Fm, are recognized as the compact asymmetric and elongated symmetric channels, while the third mode emerging for the heaviest Fm is seen to correspond to a particularly compact symmetric configuration. This result is completely in line with the experimental finding [58], as well as with the observations by other models [64, 67], which confirms the capability of the Fourier shape parametrization to describe the rich variety of shapes encountered in fission [3], as well as the accuracy of the potential-energy calculation.

We would like to emphasize at this point that this achievement of our shape parametrization was *a priori* not at all guaranteed, due to the limited number (4, actually only 3 in the present case, since the nonaxial deformation  $\eta$  plays here a rather minor role) of collective coordinates. This investigation demonstrates that the Fourier parametrization is indeed able to generate the appearance of two distinct symmetric fission valleys across the Fermium region, with properties that are supported by the experimental data. It shall be noted that the relative strength of the different fission modes cannot be deduced quantitatively from the present study. To do so, an extended range in  $q_2$  starting from before the outer saddle, and the influence of the dynamics, have to be taken into account. This is beyond the scope of this work.

Encouraged by the above achievement of the model, we propose to extend its application to still heavier elements. In particular, we are interested in investigating what happens *beyond* the abrupt change evidenced in the heavy Fm isotopes. Very little experimental information exists only up to Rf [60], due to the difficulty in accessing this region of the nuclear chart with standard methods.

The analysis of the No isotopic chain exhibits a tendency very similar to that of the Fm one: the prevalence of asymmetric fission slowly changes to favored symmetric fission between No mass 256 and 262. Similarly to Fm, depending on the fissioning system, two (for lighter No) or three (for heavier No) distinct fission paths are predicted.

Along the chain of Rf, the same kind of pattern is again observed. A few  $(q_2, q_3)$  maps were shown in Fig. 8. The  $(q_4, q_3)$  maps projected at  $q_2 = 1.75$  are displayed in Fig. 16 for two isotopes. Like for Fm and No, a second compact symmetric fission path appears for the heavier isotopes. Notice however that the outer barrier decreases below 2 MeV, when it does not nearly vanish for the

heaviest Rf isotopes displayed (see  $^{264}\text{Rf}$  in Fig. 8). The barrier disappears completely when going to still higher  $Z$  numbers. In addition, as seen for some Hs isotopes in Fig. 8, the potential-energy landscape along the descent to scission can be rather flat in the  $q_3$  direction. In spite of that softness, well-localized and well-defined valleys persist. This is demonstrated for  $^{264}\text{Rf}$  and  $^{272}\text{Hs}$  in the  $(q_4, q_3)$  maps of Fig. 16, where three distinct minima are again predicted. One concludes from this analysis that in order to localize these different fission valleys, it is absolutely essential to analyze the multidimensional energy landscape, as we have done here, and that a pure consideration of say the  $(q_2, q_3)$  map would have failed to evidence these different fission valleys.

Interestingly, it is also observed that the minimum corresponding to the elongated symmetric scission configuration tends to disappear with increasing Hs mass, and this, in favor of the compact symmetric configuration. This result suggests a new change in the picture of fission above the Fm chain. Below Fm, there is a coexistence between an asymmetric compact and a symmetric elongated mass split. In the Fm region, an additional contribution from a symmetric compact configuration emerges. For heavier elements, the pattern transforms into the coexistence of an asymmetric and a symmetric partition, where both of these correspond to a compact shape. To our knowledge the question of the evolution of fission modes beyond the Fm transition is addressed here for the first time. The new feature predicted by our model arises from the complex structure of the multidimensional potential-energy landscape. It would be very interesting to investigate our predictions both theoretically (with other models), and experimentally as a next probe of the richness of available deformation spaces and the precision of potential-energy calculations. Robust and accurate predictions are indeed of prime importance for a further extension of fission calculation in the SHE region.

#### IV. CONCLUSIONS

The recently developed four-dimensional Fourier parametrization of nuclear shapes, combined with the extensively tested and successful macroscopic-microscopic approach of the potential energy based on the Lublin-Strasbourg Drop and microscopic shell and pairing corrections, is employed to predict the properties of very heavy and super-heavy nuclei. A careful analysis of the 4D potential-energy landscapes of 324 even-even isotopes with  $92 \leq Z \leq 126$  and isospins  $40 \leq N-Z \leq 74$  allows to study the evolution with proton and neutron number of the equilibrium ground-state configuration, the possible presence of isomers, the properties of ground-state  $\alpha$ -radioactivity ( $Q_\alpha$ -value and half-life) and of spontaneous fission (barrier heights and fission half-lives). The results of our calculations have proven to reproduce the experimental data for all these observables

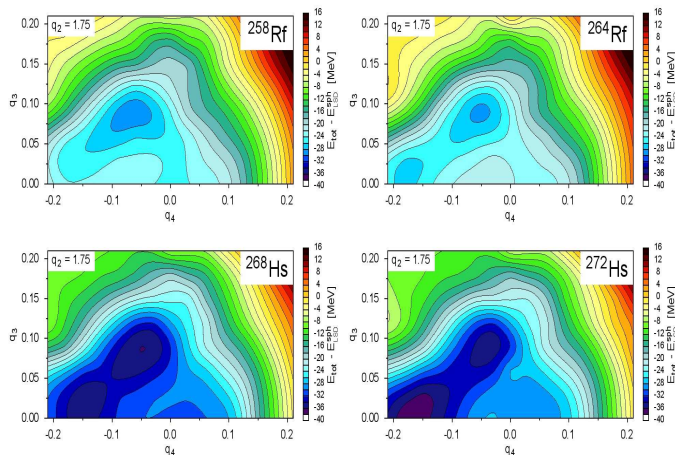


FIG. 16: (Color online) Deformation energy as in Fig. 14 at  $q_2 = 1.75$ , for  $^{258,264}\text{Rf}$  and  $^{268,272}\text{Hs}$ .

to a good accuracy, whenever such data were available. The enhanced stability of SHE with  $N = 162$ , and to a lesser extend for  $N = 152$ , is, in particular, clearly evidenced in our model results.

These calculations anticipate that nearly all investigated isotopes in the discussed region are characterized in the ground-state by axial and left-right symmetry. In general, nuclei with  $A \leq 280$  are prolate, those with  $280 \leq A \leq 300$  are spherical or transitional, while for  $Z \geq 122$  and  $A \geq 300$  oblate configuration tends to dominate. For the majority of nuclei with  $Z \leq 104$  prolate-deformed shape isomers are predicted.

The results by our model suggest that the next shell closure will appear in the vicinity of  $Z=116$  and  $N=174$

with a rather wide island of relative stabilization from  $Z \approx 114$  to  $Z \approx 118$  with  $48 \leq N - Z \leq 66$ .

The present theoretical framework is finally employed to investigate the evolution across the Fm region of the properties of possibly multiple fission paths. The abrupt change in the fragment-mass and kinetic energy distributions observed experimentally between  $^{256}\text{Fm}$  and  $^{258}\text{Fm}$ , and attributed to the appearance of “double shell-stabilized” symmetric splits, is consistent with the calculated emergence in the 4D deformation space of a fission valley leading to a compact symmetric scission configuration. The model anticipates a change in the fission mode picture beyond the Fm transition. Shell-stabilized asymmetric and symmetric channels are predicted to dominate, whereas the macroscopic-driven symmetric (super-long) partition tends to disappear. The evolution of fission modes *beyond* Fm is addressed here for the first time. Our conjecture of shell-dominated channels for fission in the vicinity of Hs would be interesting to investigate further, from the theoretical and the experimental point of view.

Altogether, the here presented achievement of the Fourier shape parametrization in a 4-dimensional deformation space, combined with reliable potential energy calculations offers an attractive basis for dynamical calculations related both with collective rotational and vibrational excitations as well as with fission.

## Acknowledgements

This work has been partly supported by the Polish-French COPIN-IN2P3 collaboration agreement under project number 08-131 and by the Polish National Science Center, grant No. 2016/21/B/ST2/01227.

- 
- [1] A. T. Kruppa, M. Bender, W. Nazarewicz, P.-G. Reinhard, T. Vertse, and S. Cwiok, Phys. Rev. **C61**, 034313 (2000).
  - [2] A. Sobczewski and K. Pomorski, Prog. Part. Nucl. Phys. **58**, 292 (2007).
  - [3] C. Schmitt, B. Nerlo-Pomorska, K. Pomorski, and J. Bartel, Phys. Rev. **C95**, 034612 (2017).
  - [4] A. Zdeb, M. Warda, and K. Pomorski, Phys. Rev. **C87**, 024308 (2013).
  - [5] Lord Rayleigh, Proc. Roy. Soc. **29**, 71 (1879).
  - [6] P. Jachimowicz, M. Kowal, and J. Skalski, Phys. Rev. C **87**, 044308 (2013).
  - [7] A. Dobrowolski, K. Pomorski, and J. Bartel, Phys. Rev. **C75**, 024613 (2007).
  - [8] J. R. Nix, Nucl. Phys. **A130**, 241 (1969).
  - [9] V. V. Pashkevich, Nucl. Phys. **A169**, 275 (1971).
  - [10] V. V. Pashkevich and A. Y. Rusanov, Nucl. Phys. **A810**, 77 (2008).
  - [11] M. Brack, J. Damgaard, A. S. Jensen, H. C. Pauli, V. M. Strutinsky, and C. Y. Wong, Rev. Mod. Phys. **44**, 320 (1972).
  - [12] K. Pomorski and J. Bartel, Int. Journ. Mod. Phys. **E15**, 417 (2006).
  - [13] S. Trentalange, S.E. Koonin, and A.J. Sierk, Phys. Rev. **C22**, 1159 (1980).
  - [14] K. Pomorski, B. Nerlo Pomorska, J. Bartel, and C. Schmitt, Acta Phys. Polon. B Sup. **8**, 667 (2015).
  - [15] K. Pomorski, B. Nerlo-Pomorska, and J. Bartel, Phys. Scr. **92**, 064006 (2017).
  - [16] A. Bohr, Kgl. Danske Vid. Selsk. Mat. Fys. Medd. **26**, 14 (1952).
  - [17] K. Pomorski and J. Dudek, Phys. Rev. **C67**, 044316 (2003).
  - [18] W.D. Myers and W.J. Swiatecki, Nucl. Phys. **A612**, 249 (1997).
  - [19] P. Moller, J. R. Nix, W. D. Myers, and W.J. Swiatecki, At. Data and Nucl. Data Tab. **59** 185 (1995).
  - [20] S. G. Nilsson, C. F. Tsang, A. Sobczewski, Z. Szymanski,



- S. Wycech, C. Gustafson, I. L. Lamm, P. Möller, and B. Nilsson, Nucl. Phys. **A131**, 1 (1969).
- [21] V. M. Strutinsky, Nucl. Phys. **A95**, 420 (1967).
- [22] A. Gozdz, and K. Pomorski, Nucl. Phys. **A451**, 1 (1986).
- [23] A. Dobrowolski, K. Pomorski, and J. Bartel, Comp. Phys. Com. **199**, 118 (2016).
- [24] K.T.R. Davies, and J.R. Nix, Phys. Rev. **C14**, 1977 (1976).
- [25] K. Pomorski, unpublished.
- [26] K. Pomorski, Comp. Phys. Comm. **174**, 181 (2006).
- [27] S. Cwiok, P.-H. Heenen, and W. Nazarewicz, Nature **433**, 705 (2005).
- [28] CEA Bruyères-le-Châtel Web site: [www-phynu.cea.fr/science.en.ligne/carte.potentiels.microscopiques/noyaux/z110/triax/z110n178triax\\_eng.html](http://www-phynu.cea.fr/science.en.ligne/carte.potentiels.microscopiques/noyaux/z110/triax/z110n178triax_eng.html).
- [29] S. Cwiok, J. Dobaczewski, P.-H. Heenen, P. Magierski, and W. Nazarewicz, Nucl. Phys. **A611**, 211 (1996).
- [30] P. Moller, A.J. Sierk, T. Ichikawa, and H. Sagawa, At. Data. and Nucl. Data Tables **109**, 1 (2016).
- [31] S. Hofmann and G. Münzenberg, Rev. Mod. Phys. **72**, 733 (2000) and references therein.
- [32] B. Nerlo-Pomorska, K. Pomorski, C. Schmitt, and J. Bartel, Phys. Scr. **90**, 114010 (2015).
- [33] P. Jachimowicz, M. Kowal, and J. Skalski, Phys. Rev. **C89**, 024304 (2014).
- [34] P. Moller, A. J. Sierk, T. Ichikawa, A. Iwamoto, R. Bengtsson, H. Uhrenholt, and S. Aberg, Phys. Rev. **C79**, 064304 (2009).
- [35] P. Moller, A. J. Sierk, T. Ichikawa, A. Iwamoto, and M. Mumpower Phys. Rev. **C91**, 024310 (2015).
- [36] Yu.Ts. Oganessian et al., Phys. Rev. Lett. **83**, 3154 (1999); **104**, 142502 (2010); Nature **400**, 242 (1999); Phys. Rev. **C62**, 041604 (2000); **C63**, 011301 (2001); **C69**, 054607 (2004); **C74**, 044602 (2009).
- [37] NUDAT Web site at <http://www.nndc.bnl.gov/nudat2/>.
- [38] A. Sobczewski, Phys. Rev. **C94**, 051302(R) (2017).
- [39] F. P. Hessberger, Eur. Phys. J. **A53**, 75 (2017).
- [40] S. A. Giuliani, and L. M. Robledo, Phys. Rev. **C88**, 054325 (2013).
- [41] S. Goriely, S. Hilaire, A. J. Koning, A. Bauswein, and H.-T. Janka., Phys. Proc. **47**, 115 (2013).
- [42] P. Jachimowicz, M. Kowal, and J. Skalski, Phys. Rev. **C95**, 014103 (2017).
- [43] A. Baran, M. Kowal, P.-G. Reinhard, L.M. Robledo, and A. Staszczak, M. Warda, Nucl. Phys. **A944**, 442 (2015).
- [44] H. Abusara, A.V. Afanasjev, and P. Ring, Phys. Rev. **C85** (2012) 024314.
- [45] R. Capote et al., At. Data. and Nucl. Data Tables **110**, 3107 (2009).
- [46] M. Dahlinger, D. Vermeulen, K.-H. Schmidt, Nucl. Phys. **A376**, 94 (1982).
- [47] G. Henning et al., Phys. Rev. Lett. **113**, 262505 (2014).
- [48] M.G. Itkis, Yu.Ts. Oganessian, and V.I. Zagrebaev, Phys. Rev. **C65**, 044602 (2002).
- [49] K. Pomorski, M. Warda, and A. Zdeb, Phys. Scr. **90**, 114013 (2015).
- [50] K. Pomorski, B. Nerlo Pomorska, M. Warda, A. Zdeb, J. Bartel, and C. Schmitt, Nuclear Theory, vol. **36**, 170 (2017), eds. M. Gaidarov, N. Minkov, Heron Press, Sofia.
- [51] A. N. Andreyev, K. Nishio, K.-H. Schmidt, Rep. Prog. Phys. **81**, 1 (2018).
- [52] U. Mosel and H. W. Schmitt, Nucl. Phys. **A165**, 73 (1971).
- [53] C. L. Zhang, B. Schuetrumpf, and W. Nazarewicz, Phys. Rev. **C94**, 064323 (2016).
- [54] B. D. Wilkins, E. P. Steinberg, and R. R. Chasman, Phys. Rev. **C14**, 1832 (1976).
- [55] U. Brosa, S. Grossmann, and A. Muller, Phys. Rep. **197**, 167 (1990).
- [56] L. Demattè, C. Wagemans, R. Barthélémy, R. D’hondt, and A. Deruytter, Nucl. Phys. **A617**, 331 (1997).
- [57] K.-H. Schmidt, B. Jurado, C. Amouroux, and C. Schmitt, Nucl. Data Sheets **131**, 107 (2016).
- [58] E. K. Hulet, J. F. Wild, R. J. Dougan, R. W. Lougheed, J. H. Landrum, A. D. Dougan, M. Schädel, R. L. Hahn, P. A. Baisden, C. M. Henderson, R. J. Dupzyk, K. Sümmerer, and G. R. Bethune, Phys. Rev. Lett. **56**, 313 (1986).
- [59] Y. Nagame and H. Nakahara, Radiochim. Acta **100**, 605 (2012).
- [60] E. K. Hulet, J. F. Wild, R. J. Dougan, R. W. Lougheed, J. H. Landrum, A. D. Dougan, P. A. Baisden, C. M. Henderson, R. J. Dupzyk, R. L. Hahn, M. Schädel, K. Sümmerer, and G. R. Bethune, Phys. Rev. **C40**, 770 (1989).
- [61] E. K. Hulet, R. W. Lougheed, J. H. Landrum, J. F. Wild, D. C. Hoffman, J. Weber, and J. B. Wilhelmy, Phys. Rev. **C21**, 966 (1980).
- [62] V. V. Pashkevich, Nucl. Phys **A477**, 1 (1988).
- [63] P. Moller, D. G. Madland, A. J. Sierk, and A. Iwamoto, Nature (London) **409**, 785 (2001).
- [64] T. Ichikawa, A. Iwamoto, and P. Moller, Phys. Rev. **C79**, 014305 (2009).
- [65] H. Pasca, A. V. Andreev, G. G. Adamian, and N. V. Antonenko, Nucl. Phys. **A969**, 226 (2017).
- [66] L. Bonneau, Phys. Rev. C **74**, 014301 (2006).
- [67] M. Warda, J. L. Egido, L. M. Robledo, and K. Pomorski, Phys. Rev. C **66**, 014310 (2002).
- [68] N. Dubray, H. Goutte, and J.-P. Delaroche, Phys. Rev. C **77**, 014310 (2008).
- [69] H. W. Schmitt, J. H. Neiler, and F. J. Walter, Phys. Rev. **141**, 1146 (1966).